

## Numerical Simulation of Dimensional Change during Austempering Heat Treatment in Ductile Cast Iron

A.D. Boccardo<sup>1\*</sup>, A.D. Sosa<sup>2,3</sup>, M.D. Echeverría<sup>2,3</sup>, P.M. Dardati<sup>1</sup>,  
D.J. Celentano<sup>4</sup>, and L.A. Godoy<sup>5</sup>

<sup>1</sup>Departamento de Ingeniería Mecánica, Universidad Tecnológica Nacional, Facultad Regional Córdoba. Maestro M. Lopez esq. Cruz Roja Argentina, Córdoba, Argentina.

<sup>2</sup>School of Engineering, Universidad Nacional de Mar del Plata, J.B. Justo 4302, Mar del Plata (B7608FDQ), Argentina.

<sup>3</sup>Metallurgy División, INTEMA, J.B. Justo 4302, Mar del Plata (B7608FDQ), Argentina.

<sup>4</sup>Departamento de Ingeniería Mecánica y Metalúrgica, Pontificia Universidad Católica de Chile. Av. Vicuña Mackenna 4860, Santiago de Chile, Chile.

<sup>5</sup>Facultad de Ciencias Exactas, Físicas y Naturales, Universidad Nacional de Córdoba, CONICET. Av. Velez Sársfield 1611, Córdoba, Argentina.

Changes in the form and dimensions of ductile iron parts occur during the austempering process, and this poses a challenge whenever tight tolerances need to be satisfied. Thus, it is important to be able to predict the deformation which occur under heat treatment to evaluate the minimum and maximum stock material required to perform the final machining. Moreover, parts could be machined before heat treatment under better machinability condition. This paper presents a thermo-mechanical-metallurgical formulation to predict the dimensional changes and final microstructure of a ductile cast iron part as a consequence of the austempering heat process. A coupled thermal, mechanical and metallurgical problem is solved using a finite element method, to take into account different coupled and complex phenomena present in this process. As an illustration, the heat treatment of a specimen is considered and results are validated by comparison with experimental data.

**Keywords:** austempered ductile iron, dimensional change, numerical simulation, finite element analysis.

### Introduction

Nodular cast iron is currently employed in industry because of its improved mechanical properties and facility to cast. Its microstructure is formed by graphite nodules which are inserted in a metal matrix. In an as-cast nodular cast iron, the matrix may be ferritic, ferritic-perlitic, or perlitic. The mechanical properties of nodular cast iron may be improved by means of an austempered heat treatment, which is the subject of this paper.

The ever growing use of austempered ductile iron (ADI) in manufacturing high strength parts, such as gears and other elements and devices of the agricultural and transport industry, has increased the interest of ADI researchers and users in several aspects of metallurgy and optimal sequence of parts manufacturing.<sup>1-5</sup>

To perform an austempering treatment, the material is initially heated and kept at a temperature between 1123K and 1223K in order to obtain a matrix which is completely austenitic and with the appropriate carbon contents. Next, the material is suddenly cooled down to a temperature between 523K and 723K to initiate the austempering process. The chosen temperature for the treatment depends on the desired microstructure (lower or upper bainitic ferrite). Finally, the part is cooled until ambient temperature is reached.<sup>5,6</sup>

As a consequence of the heat treatment process, there are changes in the part dimensions.<sup>4,7</sup> In several experimental reports, the influence of chemical composition, part shape, austenized and austempered temperature, initial matrix, and density of graphite nodules on the change of dimensions have been observed.<sup>2,4,7,8</sup> Parts with ferritic initial matrix undergo smaller changes in dimensions than those based on an initially perlitic matrix. Therefore, in some applications, parts with an initial perlitic matrix are subjected to a ferritic treatment prior to an austempering treatment.<sup>4</sup> Parts with high graphite nodule density experience large changes.<sup>8</sup>

The quantitative prediction of dimensional change (DC) plays a key role in the mass production of parts, because it allows not only performing final machining before heat treatment under better machinability conditions but also allows obtaining parts with the required dimensional tolerances.

Taking the data from experimental studies into account, Dai Pra *et al.* developed a fuzzy model to predict DC% values, involving ten typical parameters corresponding to chemical composition and thermal cycle. The predictions confirmed the experimental information; and relevant data concerning the individual effects of the alloying elements and

---

\* Corresponding author, email: aboccardo@mecanica.frc.utn.edu.ar

relative compositions were obtained, not available in systematic studies previously reported.<sup>9</sup> There are models which allow predicting residual stresses and the final shape of nodular cast iron parts following solidification and subsequent cooling down to the ambient temperature<sup>10-12</sup>, but no models have yet been developed for the parts which have been subjected to austempering treatment.

This paper presents a thermo-mechanical-metallurgical formulation to represent the austempering heat treatment process of a nodular cast iron. The model allows predicting phase fractions, final shape, and residual stresses in a part, by taking into account the initial microstructure, chemical composition, temperature of the thermal process, and initial shape of the part.

The thermo-mechanical-metallurgical formulation is first presented, followed by results of experiments carried out to validate the computational tools. Details of the implementation of the model are provided.

### Thermo-mechanical-metallurgical formulation

The heat treatment process to obtain an ADI may be modeled by taking into account thermal, mechanical, and metallurgical problems. The thermal problem considers the temperature evolution; the mechanical problem accounts for strain and stress evolution due to heating, cooling and phase change; whereas the metallurgical problem deals with the evolution of the phase in the material. Those are interdependent problems, as shown in Fig. 1.

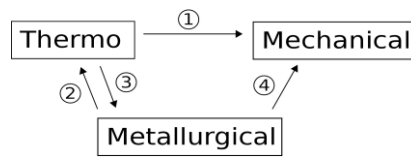


**Fig.1:** Interactions between thermal, mechanical and metallurgical problems.

The mechanical model receives information concerning temperature and phase change through interactions 1 and 4 in Fig. 1, which is used in the computation of strains and stresses. Interaction 2 accounts for the thermal problems, the heat liberation or absorption produced during phase change. The phase change is related to temperature through interaction 3.

### Thermo-mechanical model

A fully coupled thermal-stress analysis in ABAQUS standard was used in this work. The temperatures are integrated using a backward-difference scheme, and the nonlinear coupled system is solved using Newton's method.<sup>13</sup> An exact implementation of Newton's method involves a non-symmetric Jacobian matrix, where the coupled equations are:

$$\begin{bmatrix} k_{uu} & k_{u\theta} \\ k_{\theta u} & k_{\theta\theta} \end{bmatrix} \begin{Bmatrix} \Delta u \\ \Delta \theta \end{Bmatrix} = \begin{Bmatrix} R_u \\ R_\theta \end{Bmatrix} \quad (1)$$

Solving this system of equations requires the use of the unsymmetric matrix storage and solution scheme. The mechanical and thermal equations must be solved simultaneously.

Implementation of interactions 1 and 4 was archived by using the general formulation for a fully solid material, which states that the total mechanical strain may be written as the sum of elastic, viscoelastic, thermal and phase change contributions<sup>14</sup>:

$$\varepsilon_{ij} = \varepsilon_{ij}^{el} + \varepsilon_{ij}^{vp} + \varepsilon_{ij}^{th} + \varepsilon_{ij}^{pc} \quad (2)$$

For an isotropic solid material, the thermal strain tensor is evaluated with equations 3. The strains due to reverse eutectoid transformation<sup>14</sup> and bainitic transformation<sup>15</sup> are evaluated with equations 4 and 5 respectively. These equations have been implemented in ABAQUS by means of a subroutine called UEXPAN.

$$\varepsilon_{ij}^{th} = \alpha_i (T - T_{ref}) \delta_{ij} \quad (3) \quad \varepsilon_{ij}^{pc} = \beta_{pc} f_{pc} \delta_{ij} / 3 \quad (4) \quad \varepsilon_{ij}^{pc} = \frac{1}{3} \left( 1 - \frac{a_\gamma^3}{\beta + a_{e\gamma}^3} \right) \delta_{ij} \quad (5)$$

$$\beta = \frac{2a_\alpha^3 - a_{e\gamma}^3}{1 + (2V_\gamma a_\alpha^3) / (V_{cb} a_{e\gamma}^3)} \quad (6)$$

The interaction 2 is taken into account through evaluation of phase change heat flow with equation 7, which is implemented in subroutine HETVAL.<sup>16</sup>

$$r = L \rho f_{pc} \quad (7)$$

**Metallurgical model**

A reverse eutectoid transformation occurs during heating of a part starting at ambient temperature up to the austenized temperature, during which an initial ferritic-perlitic matrix is transformer into austenite. As a following stage, during cooling from austenized to austemperized, as the temperature becomes lower than bainite start, there is a bainitic transformation. During this bainitic transformation, part of the austenite is transformed into a bainitic ferrite. Finally, during the subsequent cooling to ambient temperature, the possibility of the existence of a martensitic transformation is considered.

The model that takes the above mentioned transformations into account has been implemented in subroutine USDFLD in ABAQUS. Interaction 3 has been taken into account by means of subroutine GETVRM.

**Reverse eutectoid transformation**

The reverse eutectoid transformation is modeled by considering stable and metastable transformation.<sup>17</sup> The initial microstructure is formed by graphite nodules, ferrite halos and perlite colonies of diverse sizes. For the stable transformation, for each size of graphite nodules, a representative volume element (RVE) formed by a graphite nodule surrounded by a ferrite shell is considered.<sup>18</sup> In the metastable transformation, for each perlite colony, a RVE is formed by half layer of cementite and half of the ferrite<sup>19</sup> (see Fig. 2).

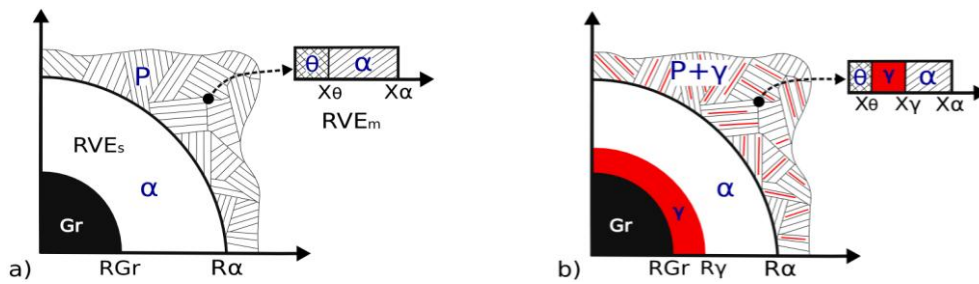


**Fig.2:** RVE employed to model the stable reverse eutectoid transformation (RVEs) and metastable reverse eutectoid transformation (RVEm). Schematic representation of phases (a) before transformation; (b) during transformation.

The model for stable reverse eutectoid transformation discussed above predicts the evolution of graphite, ferrite, and austenite fractions, by accounting for the graphite nodule size, ferrite shell, and chemical composition of the alloy. The transformation starts when the temperature reaches a value  $T_{\alpha}^o$ .<sup>20</sup> Austenite nucleation occurs at the graphite-ferrite interphase.<sup>18</sup> Instantaneous nucleation of an austenite shell of radius 1% larger than the graphite nodule is considered. The mechanism of growth is governed by long range carbon diffusion from graphite to ferrite through the interfaces graphite-austenite and austenite-ferrite.

On account of the families of equal size graphite nodules, the graphite, austenite, and ferrite fractions may be written as:

$$V_{Gr} = \frac{4\pi}{3} \sum_{i=1}^{nfam} N_{nfam_i} r_{Gr_i}^3 \quad (8) \quad V_{\gamma s} = \frac{4\pi}{3} \sum_{i=1}^{nfam} N_{nfam_i} (r_{\gamma_i}^3 - r_{Gr_i}^3) \quad (9) \quad V_{\alpha} = \frac{4\pi}{3} \sum_{i=1}^{nfam} N_{nfam_i} (r_{\alpha_i}^3 - r_{\gamma_i}^3) \quad (10)$$

The increment of graphite and austenite radius for each family size are computed through the mass balance condition for carbon at the mobile interfaces graphite-austenite and austenite-ferrite is considered, together with carbon diffusion in steady state, and mass conservation of carbon in the RVE, in the form:

$$\frac{dr_{Gr_i}}{dt} = \frac{D_{\gamma} \rho_{\gamma} r_{\gamma_i}}{r_{Gr_i} (r_{\gamma_i} - r_{Gr_i})} \frac{(C_{\gamma/\alpha} - C_{\gamma/Gr})}{(C_{Gr} \rho_{Gr} - C_{\gamma/Gr} \rho_{\gamma})} \quad (11)$$

$$\frac{dr_{\gamma_i}}{dt} = \frac{D_{\alpha} \rho_{\alpha} r_{\alpha_i}}{r_{\gamma_i} (r_{\alpha_i} - r_{\gamma_i})} \frac{(C_{as} - C_{\alpha/\gamma})}{(C_{\gamma/\alpha} \rho_{\gamma} - C_{\alpha/\gamma} \rho_{\alpha})} - \frac{D_{\gamma} \rho_{\gamma} r_{Gr_i}}{r_{\gamma_i} (r_{\gamma_i} - r_{Gr_i})} \frac{(C_{\gamma/\alpha} - C_{\gamma/Gr})}{(C_{\gamma/\alpha} \rho_{\gamma} - C_{\alpha/\gamma} \rho_{\alpha})} \quad (12)$$

$C_{\gamma/\alpha}$  and  $C_{\alpha/\gamma}$  are evaluated using expressions given by Lacaze and Gerval.<sup>21</sup>  $C_{\gamma/Gr}$  is computed with expressions given by Boeri.<sup>22</sup>

The model of the metastable reverse eutectoid transformation predicts the evolution of the perlite and austenite fractions, and takes into account the inter-laminar spacing of perlite colonies and the chemical composition of the alloy. The transformation starts when the temperature reaches the higher of  $T_p$  or  $T_{\alpha}$ .<sup>20</sup> Nucleation and growth of austenite occurs at the cementite-ferrite interface<sup>19</sup>. Instantaneous nucleation is considered of an austenite layer with a thickness

equal to 1% of the cementite layer. The growth mechanism is governed by long-range carbon diffusion, from cementite to ferrite, through the interfaces cementite-austenite and austenite-ferrite.

Perlite and austenite fractions are calculated for different perlite colonies, as:

$$V_p = \sum_{j=1}^{ncol} V_{col_j} \left[ 1 - \frac{2(x_{\gamma_j} - x_{\theta_j})}{sip_j} \right] \quad (13) \quad V_{\gamma m} = 2 \sum_{j=1}^{ncol} V_{col_j} \frac{(x_{\gamma_j} - x_{\theta_j})}{sip_j} \quad (14)$$

The mass balance condition for carbon at the mobile interfaces cementite-austenite and austenite-ferrite is considered, together with carbon diffusion in steady state, and mass conservation of carbon in the RVE, in order to evaluate the increment of position of interfaces in the form:

$$\frac{dx_{\theta_j}}{dt} = \left( \frac{D_{\gamma} \rho_{\gamma}}{x_{\gamma_j} - x_{\theta_j}} \right) \frac{(C_{\gamma/\alpha} - C_{\gamma/\theta})}{(C_{\theta} \rho_{\theta} - C_{\gamma/\theta} \rho_{\gamma})} \quad (15)$$

$$\frac{dx_{\gamma_j}}{dt} = \left( \frac{D_{\alpha} \rho_{\alpha}}{x_{\alpha_j} - x_{\gamma_j}} \right) \frac{(C_{am} - C_{\alpha/\gamma})}{(C_{\gamma/\alpha} \rho_{\gamma} - C_{\alpha/\gamma} \rho_{\alpha})} - \left( \frac{D_{\gamma} \rho_{\gamma}}{x_{\gamma_j} - x_{\theta_j}} \right) \frac{(C_{\gamma/\alpha} - C_{\gamma/\theta})}{(C_{\gamma/\alpha} \rho_{\gamma} - C_{\alpha/\gamma} \rho_{\alpha})} \quad (16)$$

$C_{\gamma/\theta}$  is evaluated with an equation proposed by Kapturkiewicz *et al.*<sup>19</sup>

The total austenite fraction is computed by means of the sum of austenite fraction formed during the stable and metastable transformations:

$$V_{\gamma} = V_{\gamma s} + V_{\gamma m} \quad (17)$$

### Bainitic Transformation

The model employed for the bainitic transformation allows computation of bainitic ferrite and residual austenite. The carbon mass in graphite nodule is assumed to be constant, with the consequence that the graphite volume fraction remains constant<sup>23</sup>. The kinetics of growth of bainitic ferrite is modeled by means of Avrami's equation<sup>24</sup>, equation (18). The maximum fraction of bainitic ferrite is computed using the lever-rule<sup>5</sup>, equation (19). The residual austenite fraction is computed from equation (20).

$$V_{ab} = V_{ab}^{max} \left[ 1 - \exp(-k_a t^{m_a}) \right] \quad (18) \quad V_{ab}^{max} = (1 - V_{Gr}) (C_{\gamma To} - C_{\gamma}) / (C_{\gamma To} - C_{ab}) \quad (19) \quad V_{\gamma} = 1 - (V_{Gr} + V_{ab}) \quad (20)$$

### Martensitic Transformation

The martensitic transformation occurs when the temperature martensite start ( $M_s$ ) is higher than the ambient temperature<sup>5</sup>. The temperature  $M_s$  depends on the concentration of alloy components in the residual austenite. The carbon concentration plays an important role because the latter increases as the bainitic transformation progresses. Thus,  $M_s$  is inversely proportional to austempered time.

The model employed for the martensite transformation evaluates  $M_s$  once cooling starts from the austempered temperature to ambient temperature. If  $M_s$  is higher than the ambient temperature, then part of the residual austenite is transformed into martensite. The residual austenite that did not become martensite is known as retained austenite. The volume fractions of martensite<sup>25</sup> and retained austenite are computed by equations (21) and (22).

$$-\ln(1 - V_{\alpha'}) / V_{\alpha'} = 1 + c_2 (M_s - T) \quad (21) \quad V_{\gamma} = 1 - (V_{Gr} + V_{ab} + V_{\alpha'}) \quad (22)$$

## Experimental Procedure

Twelve cylindrical coupons, having 10mm diameter and 100mm length, were tested as a part of this research. The chemical composition of the coupons is given in table 1.

**Table 1:** Chemical Composition [w%]

Melt	C	Si	Mn	Mg	Cu	P, S	EC
A	3.36	3.13	0.32	0.5	0.25	0.25	4.4
B	2.81	3.54	0.36	0.64	0.11	0.24	4
C	2.64	4.2	0.36	0.62	0.11	0.24	4

The temperatures of austenization were  $T_{\gamma A}=1173\text{K}$ ,  $T_{\gamma B}=1193\text{K}$  y  $T_{\gamma C}=1213\text{K}$  for the three chemical compositions A, B y C respectively. In all tests, the austempered temperature was  $T_{\alpha}=633\text{K}$ , and the time was 90 minutes.

All dimensions were measured before and after heat treatment. A millesimal outside micrometer (0-25mm) of accuracy  $\pm(1+L/75)\mu\text{m}$  was used to measure the cylindrical samples diameter. The length was measured with a Coordinate Measuring Machine of accuracy  $\pm(1.2+ L/1000)\mu\text{m}$ . To achieve greater repeatability in measurements, special supports were used, which allowed fixing specimens in same position before and after heat treatment.

The metallographic characterization of the specimens before and after heat treatment was performed using conventional methods of inclusion and polishing. The polished surfaces were etched with nital 2%. The microstructures were analyzed using an Olympus PMG3 optical microscope; and the proportions of the phases in each sample were quantified by means of image software.

In all cases, castings displayed a nodule size 5, nodularity higher than 80%. The nodule count and phase fractions in as-cast condition are given in table 2. As expected, as Si content increased, the amount of ferrite in the as-cast microstructure also increased. Fig. 3 depicts the representative microstructures under as-cast condition for each melt under study.

**Table 2:** Nodule count [nodules  $\text{m}^{-3}$ ] and phase fractions [%] in as-cast condition

Melt	nodule count	$V_{Gr}$	$V_{\alpha}$	$V_P$
A	$1.563 \times 10^{12}$	9	39.5	51.5
B	$2.164 \times 10^{12}$	11.4	68.9	19.7
C	$1.822 \times 10^{12}$	10.5	79.5	10

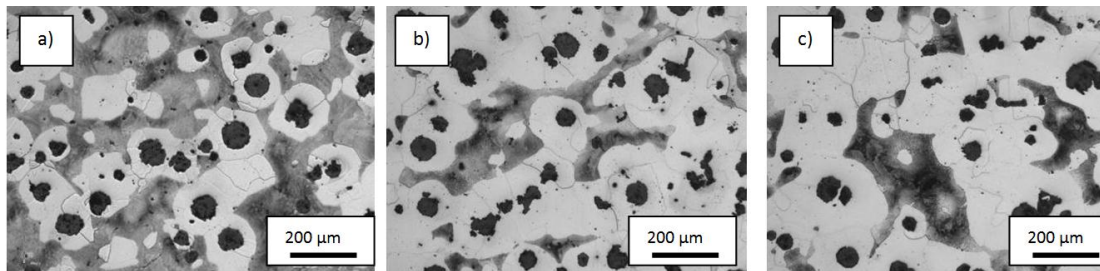


**Fig. 3:** Microstructures in as-cast condition: (a) melt A, (b) melt B, and (c) melt C.

The X-ray diffraction patterns (XRD) corresponding to the different  $\{hkl\}$  reflections in ferrite and austenite phases were measured in ADI samples to estimate the amount of austenite and its carbon content. Graphite-monochromated  $\text{Co-K}\alpha$  radiation ( $\lambda=0.1789\text{nm}$ ) was the option of choice for such measurement. The X-ray tube was operated at 40kV and 30mA. Three XRD intensity patterns versus  $2\theta$  were obtained for each ADI sample, and a scan in the range of  $47^\circ$  to  $62^\circ$  with a  $2\theta$  step of  $0.05^\circ$  and 0.05 seconds by step was performed. Powder Cell software developed by Kraus and Nolz<sup>26</sup>, for peak profile refinement was applied to analyze the XRD patterns and to obtain peak positions and intensities as well as austenite volume fraction and its lattice parameter.

The percentage variations of other phases, such as non-retained austenite and/or carbides, were disregarded as they are believed not to affect  $V_{\gamma}$  and  $C_{\gamma}$  estimations.

The percent dimensional change ( $DC_i$ ) was calculated using the measured dimensions values before and after each austenitizing-austempering heat treatment based on expression (23). The arithmetic mean of  $DC_i$  ( $DC_{Mean}$ ) and its dispersion ( $\Delta DC$ ) were calculated for each group of specimens from a melting-heat treatment batch using Equations (24) and (25).

$$DC_i = \frac{(l_f - l_o)}{l_o} 100 \quad (23) \quad DC_{Mean} = \frac{1}{n} \sum_{i=1}^n DC_i \quad (24) \quad \Delta DC = \sqrt{\frac{1}{n-1} \sum_{i=1}^n (DC_i - DC_{Mean})^2} \quad (25)$$

### Numerical Procedure

The specimen described in the experimental procedure was heat treated using the proposed formulation. Owing to the symmetry, half sample was discretized using 250 axisymmetric elements of 8 nodes. The thermo-mechanical-microstructural properties of nodular cast iron are listed in table 3. The thermal properties of casting/bath salt interface are listed in table 4 and thermal properties of casting/furnace and casting/environment interfaces are listed in table 5.

**Table 3:** Thermo-mechanical-microstructural properties of nodular cast iron.<sup>5,12,15,17</sup>

Temp [K]	Young's Modulus [MPa]	Yield strength [MPa]		
293	163500	260		
773	110900	130		
1273	28400	20		
Poisson's ratio: 0.33				
Thermal dilatation [K <sup>-1</sup> ]: $\alpha_{\text{t\alpha p}} = 14 \times 10^{-6}$ (ferrite and perlite); $\alpha_{\text{t\gamma}} = 25.61 \times 10^{-6}$ (austenite); $\alpha_{\text{t\alpha b}} = 13.5 \times 10^{-6}$ (bainitic ferrite)				
Lattice parameters at ambient temperature [ $1 \times 10^{-10}$ m]: $a_{\alpha\text{o}} = 2.873$ ; $a_{\gamma\text{o}} = 3.555 + 0.04C_{\gamma\text{o}}$				
Eutectoid reverse phase change volumetric deformation: $\beta_{\text{pc}} = -6.22 \times 10^{-4}$				
Temp [K]	Conductivity [W m <sup>-1</sup> K <sup>-1</sup> ]	Specific heat [J kg <sup>-1</sup> K <sup>-1</sup> ]		Density [kg m <sup>-3</sup> ]
293	44.1	500		7277
833	37.1	750		7120
1253	22.5	820		7070
Latent heat of reverse eutectoid transformation [J kg <sup>-1</sup> ]: $L_{\text{p}} = 9 \times 10^4$ (perlite); $L_{\alpha} = 4 \times 10^4$ (ferrite)				
Avrami's parameters: $k_{\alpha} = 0.032617$ ; $m_{\alpha} = 1.2146$				

**Table 4:** Thermal properties of casting/bath salt interface.

Temp [K]	Heat transfer coefficient [J s <sup>-1</sup> m <sup>-2</sup> K <sup>-1</sup> ]
473	250
573	400
773	3000
1223	10

**Table 5:** Thermal properties of casting/furnace and casting/environment interfaces.<sup>17</sup>

Interface	Heat transfer coefficient [J s <sup>-1</sup> m <sup>-2</sup> K <sup>-1</sup> ]
Casting/furnace	70
Casting/environment	70

## Results and Discussion

The formulation presented before was used to describe the thermo-mechanical-metallurgical response of the ADI used in the experiments. The evolution of computed phases for the melt A is presented in Fig. 5a. The phases at the end of the heat treatment are included in table 6. The model predicts that martensite is not present; this is in agreement with the experiments because the micrographs obtained following austempered do not show martensite in the material. The matrix from micrographs is composed of ausferrite (96%) and retained austenite (4%).

**Table 6:** Computed phase fractions [%] obtained with the heat treatment.

Melt	V <sub>Gr</sub>	V <sub>ab</sub>	V <sub>γ</sub>	V <sub>α'</sub>
A	8.46	49.63	41.91	0
B	6.67	46.01	47.32	0
C	6.17	42.06	51.77	0

Effects due to Si content in phase fractions are observed: A decrease in the quantity of Si produces an increase in the fraction of bainitic ferrite, while the fraction of retained austenite decreases. This is due to (a) the concentration of carbon at equilibrium in austenite at the austenized temperature is virtually the same for all casts considered; and (b) the carbon concentration in residual austenite for which the bainitic transformation ( $C_{\gamma\text{T0}}$ ) is arrested, increases as the quantity of Si decreases.

The dimensional changes (length and diameter) of the coupon are shown in Fig. 4; both variations were obtained via testing and simulation. The evolution of computed longitudinal displacement of the end of half cylinder for the three melts is presented in Fig. 5b.

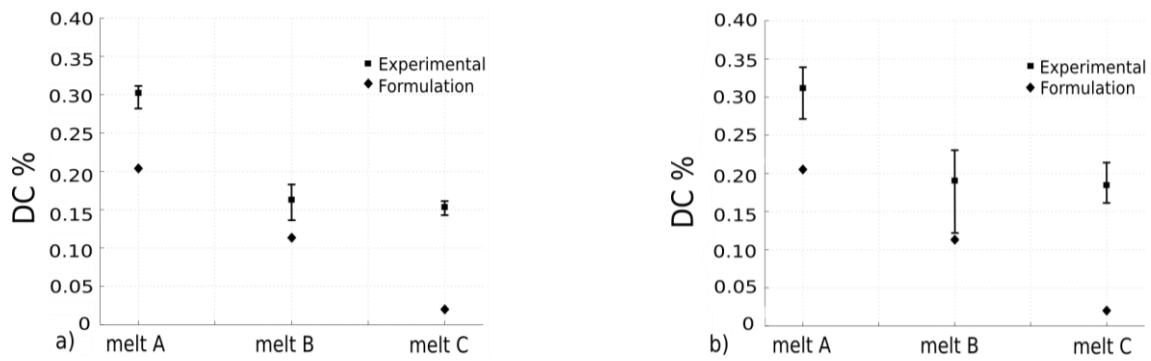


Fig.4: Dimensional change (a) length; and (b) diameter of the coupon.

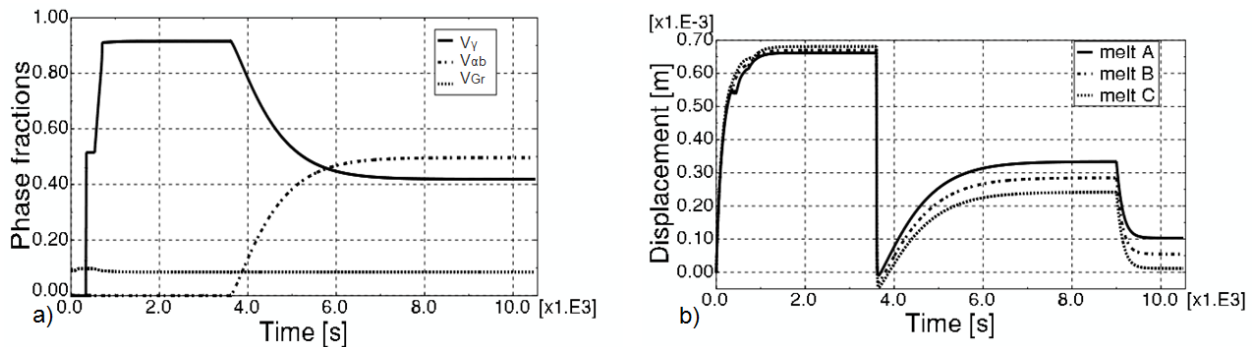


Fig.5: Evolution of computed phases for melt A (a) and evolution of computed longitudinal displacement of the end of half cylinder for three melts (b).

Next, the influences of the Si contents and initial geometry on the change in geometry were investigated. In the experiments it is possible to observe that an increase in Si concentration has the effect of reducing the changes in the geometry of the part. The Si content has an effect on the type of matrix of the cast material. By increasing the quantity of Si it is possible to obtain a matrix with higher ferrite contents. As mentioned before, other authors reported a less significant change in geometry in parts with ferritic matrix.<sup>4</sup> Other aspect to be taken into account is that an increase in Si contents yields a lower volume fraction of bainitic ferrite and lower carbon concentration in residual austenite during the bainitic transformation; this combination has the effect of a lower expansion in the part.<sup>15</sup>

The results of the computational simulation follow the same trend, with differences of 30%, 30% and 80% (for casts A, B, C, respectively) with respect to the experiments.

In the testing performed in this research the coupon diameter had larger relative changes than the length. The trend is not detected in the simulations. It may be convenient to perform new experiments with coupons of different geometries to better understand this effect.

## Conclusions

A thermo-mechanical-metallurgical formulation has been presented to simulate the austempering treatment of a nodular cast iron. The model predicts phase fractions, final shape, residual stresses, taking into account the initial microstructure, chemical composition, temperature of heat treatment, and initial shape of the part.

The model was employed to simulate the results of an austempering heat treatment of cylindrical coupons. The response was investigated to account for different initial microstructures, chemical compositions and temperatures of the process.

Comparison between experiments and computations show that the model is sensitive to the parameters which were considered in the experiments. The calculated changes in geometric dimensions in the model are considered to be adequate for the melts A and B. For the melt C it is necessary a better model for take into account interactions 1 and 4.

As further work, testing new coupons with differences in geometry will be done to investigate the influence of the initial shape in more detail.

## List of symbols

$\alpha_{ti}$	coefficient of thermal expansion of ductile iron with matrix $i$ (tangent), $K^{-1}$
$a_{\alpha,\gamma,\epsilon\gamma}$	lattice parameter of ferrite, austenite and carbon enriched austenite at the transformation temperature, m
$\beta_{pc}$	phase change volumetric deformation

$C_{\gamma/\alpha,\gamma/Gr,\gamma/\theta}$	equilibrium carbon concentration of austenite at austenite-ferrite, austenite-graphite and austenite-cementite interface respectively, wt%
$C_{\gamma,\gamma To,ab}$	average carbon concentration of austenite prior to bainitic transformation, residual austenite when bainitic transformation stops and bainitic ferrite respectively, wt%
$C_{Gr,\theta}$	carbon concentration of graphite and cementite respectively, wt%
$C_{\alpha/\gamma}$	carbon concentration of ferrite at ferrite-austenite interface, wt%
$C_{as,am}$	carbon concentration of ferrite in $r_{\alpha}$ and $x_{\alpha}$ respectively, wt%
$c_2$	parameter of martensite transformation
$D_{\gamma,\alpha}$	diffusion coefficient of carbon in austenite and ferrite respectively, $m^2 s^{-1}$
$DC$	dimensional change
$\Delta u, \Delta \theta$	corrections to the incremental displacement and temperature respectively
$\Delta DC$	dispersion of dimensional change
$\delta_{ij}$	Kronecker delta
$\varepsilon, \varepsilon^{el, vp, th, pc}$	mechanical, elastic, viscoelastic, thermal and phase change strain tensor respectively
$\rho, \rho_{\gamma,\alpha,Gr,\theta}$	density of nodular cast iron, austenite, ferrite, graphite and cementite respectively, $kg m^{-3}$
$f_{ph}$	phase change function
$k_a, m_a$	Avrami's parameters
$k_{ij}$	submatrices of the fully coupled Jacobian matrix
$L$	latent heat, $J kg^{-1}$
$l_{o,f}$	initial and final length respectively, m
$M_s$	temperature martensite start, K
$ncol, nfam$	number of colonies of perlite and number of families of graphite nodule
$N_{nfam}$	number of nodule for unit of volume of a family, $nodule m^{-3}$
$r_{Gr,\gamma,\alpha}$	radius of graphite nodule, austenite shell and ferrite halo respectively, m
$R_{u,\theta}$	mechanical and thermal residual vectors respectively
$sip$	inter pearlite spacing, m
$T_{ref}$	reference temperature, K
$V_{Gr,\alpha,P,\gamma,ab,a',col}$	volume fraction of graphite, ferrite, perlite, austenite, bainitic ferrite, martensite and a perlite colony respectively
$V_{\gamma s,\gamma m}$	volume fraction of austenite formed in the stable and the metastable reverse eutectoid transformation respectively
$x_{\theta,\gamma,\alpha}$	coordinate of cementite-austenite, austenite-ferrite and ferrite interface respectively, m

## References

1. J.R. Keough: AFS Proceeding of the 3rd World Conference on ADI, 1991, 2, 638.
2. O.J. Moncada, R.H. Spicacci and J.A. Sikora: *AFS Trans.*, 1998, 106, 39-45.
3. M.D. Echeverría, O.J. Moncada and J.A. Sikora: *ISIJ International*, 2001, 41, 25.
4. A.D. Sosa, M.D. Echeverría and O.J. Moncada: *ISIJ International*, 2004, 44, (7), 1195-1200.
5. M.A. Yescas-González: 'Modelling the microstructure and mechanical properties of austempered ductile iron', PhD thesis, University of Cambridge, Cambridge, UK, 2001.
6. D.C. Putman and R.C. Thomson: *Int. J. Cast. Met. Res.*, 2003, 16, (1-3), 191-196.
7. O. Moncada and J.A. Sikora: *AFS Trans.*, 1996, 104, 577-580.
8. A.D. Sosa, M.D. Echeverría, O.J. Moncada, N. Míngolo and J.A. Sikora: *Journal of Materials Processing Technology*, 2009, 209, 5545-5551.
9. A.L. Dai Pra, M.D. Echeverria, A. Scandurra, O.J. Moncada and J.A. Sikora: *Lat. Am. appl. res. (LAAR)*, 2005, 35, 197.
10. D. Celentano: *Int. J. Plast.*, 2001, 17, 1623-1658.
11. D. Celentano: *Mater. Manuf. Processes*, 2010, 25, (7), 546-556.
12. D.J. Celentano, P.M. Dardati, F.D. Carazo and L.A. Godoy: *Mater. Sci. Technol.*, 2013, 29, (2), 156-164.
13. Abaqus analysis user manual. 6.5.4 Fully coupled thermal-stress analysis.
14. J. A. Dantzing and M. Rappaz: 'Solidification', 1st edn, 2009, Switzerland, EPFL Press.
15. H.K.D.H Bhadeshia, S.A. David, J.M. Vitek and R.W. Reed: *Mater. Sci. Technol.*, 1991, 7, 686-689.
16. D.M. Stefanescu: 'Science and engineering of casting solidification', 2nd edn, 2009, New York, USA.
17. F.D. Carazo, P.M. Dardati, D.J. Celentano and L.A. Godoy: *Metallurgical and Materials Transactions B*, 2012, 43, (6), 1579-1595.

## 10<sup>th</sup> International Symposium on the Science and Processing of Cast Iron – SPC110

18. U. Batra, S. Ray and S.R. Prabhakar: *Journal of Materials Engineering and Performance*, 2005, 14, (5), 574-581.
19. W. Kapturkiewicz, E. Fraś and A.A. Burelko: *Materials Science and Engineering A*, 2005, 413-414, 352-357.
20. R.M. Ghergu, J. Sertucha, Y. Thebault and J. Lacaze: *ISIJ International*, 2012, 52, (11), 2036-2041.
21. J. Lacaze and V. Gerval: *ISIJ International*, 1998, 37, (7), 714-722.
22. R. Boeri: 'The solidification of ductile cast iron', PhD thesis, University of British Columbia, Canada, 1989.
23. W. Kapturkiewicz, A.A. Burelko and E. Fraś: *Int. J. Cast. Met. Res.*, 2003, 16, (1-3), 287-292.
24. U. Batra, S. Ray and S.R. Prabhakar: *Journal of Materials Engineering and Performance*, 2004, 13, (1), 64-68.
25. S.A. Khan and H.K.D.H Bhadeshia: *Materials Science and Engineering A*, 1990, 129, 257-272.
26. W. Kraus and G. Nolze. Powder Cell 2.3 version, 1998, CPD Newsletter, 20, 274.

### **Acknowledgement**

A.D. Boccardo had a doctoral scholarship from CONICET during this research. L.A. Godoy and A.D. Sosa are members of the research staff of CONICET. D.J. Celentano gratefully acknowledges the support of Fondecyt Project 1130404.